Ionospheric monitoring using GNSS data from LEO satellites for space weather applications

Additional thesis

Maurice van Tiggelen

Technische Universiteit Delft

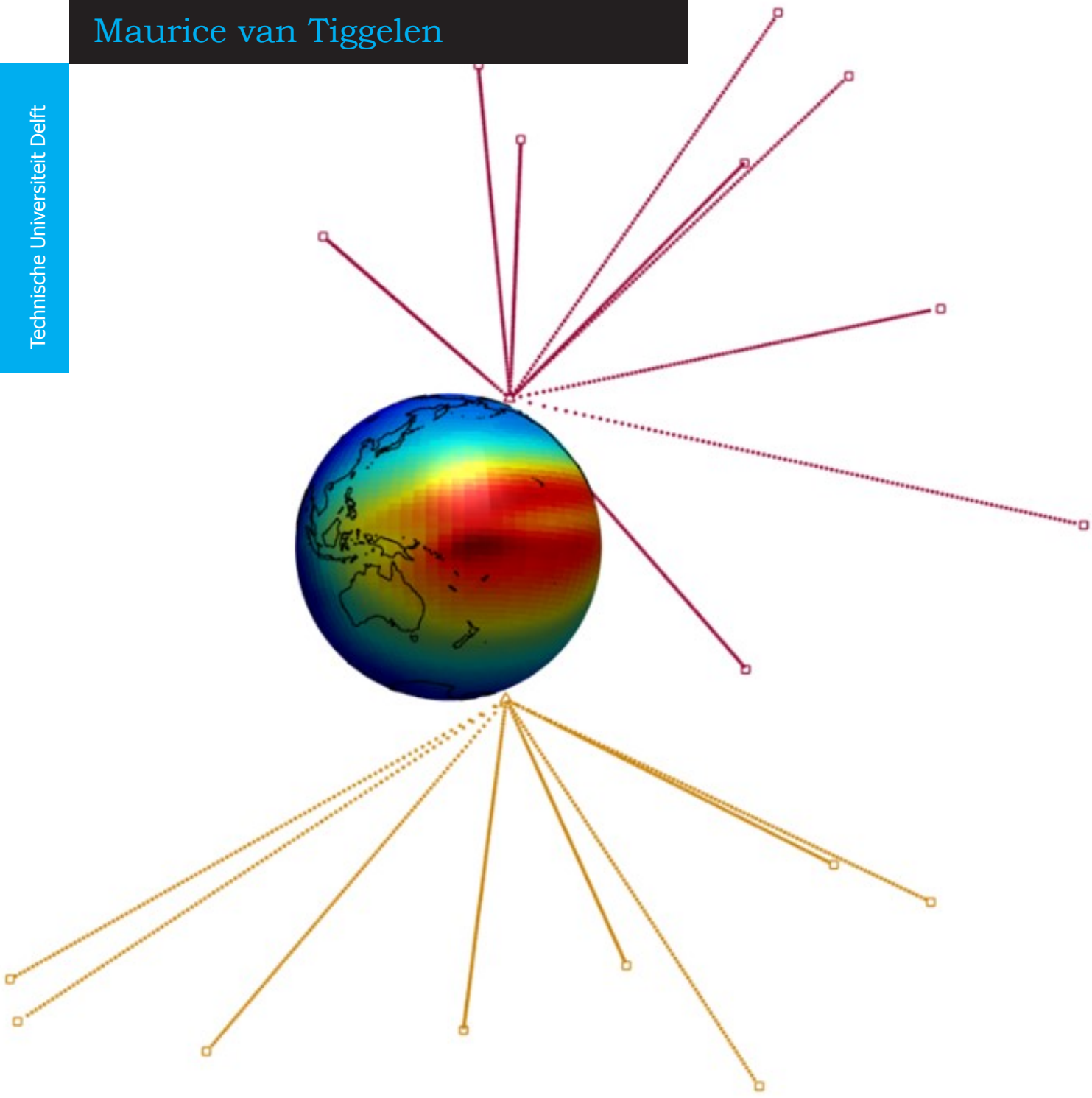

TU Delft Delft University of Technology

Challenge the future

Ionospheric monitoring using GNSS data from LEO satellites for space weather applications

Additional thesis

by

Maurice van Tiggelen
maurice.van-tiggelen@grenoble-inp.org

This work is a part of the curriculum of the Master of Science (MSc.)

"Geoscience and Remote Sensing"

at the Delft University of Technology,
submitted on March 22, 2017.

Supervisors: Dr. ir. A. A. Verhagen, TU Delft
Prof. dr. A. P. Siebesma TU Delft

Cover page: IRI-2012 model for total integrated electron content above 600km altitude on 16-03-2015 00:00 UTC and GPS to satellite wavepath geometries of the GNSS signal for the SWARM-A satellite (yellow) and GRACE-A satellite (purple).

TU Delft Delft University of Technology

Abstract

In this report, a least-squares approach is described for retrieving the 3D structure of the electron concentration in the Earth's upper ionosphere and plasmasphere, using Global Navigation Satellite System (GNSS) data-sets from Low-Earth-Orbiting (LEO) satellites. Due to the lack of horizontal radio wave geometries, the method uses assumptions on the vertical electron concentration for the retrieval of the 3D electron concentration. The first results show that this method is capable of finding small patterns of electron concentration in the horizontal direction that are not resolved in the widely used IRI model. Furthermore, the consistency of this method was proved by using several independent data sources. Finally some challenges are presented and some suggestions are made for improved retrieval of global 3D electron concentrations in future research, which can be then be used to increase the quality of space weather assimilation and GNSS ionospheric delay corrections.

Contents

1

Introduction

1.1. The Earth's Ionosphere and Plasmasphere

Historically, the ionosphere is defined as the region of the atmosphere where the concentration of free-electrons is large enough to affect radio signals. It's existence was first established with inter-Atlantic radio communications between Cornwall, England, and Newfoundland, Canada by Marconi in 1901. Today, the ionosphere is generally defined as "a partially ionized gas that surrounds the Earth and in some sense forms the interface between the atmosphere and space" [1].
Part of the photons emitted by the sun reaches the Earth and interacts with the atoms and molecules from Earth's neutral atmosphere (He, O, N2, O2, ...). The interaction, referred to as photo-ionization, dissociates positively charged ions and electrons through the absorption of photons. The recombination of ions and electrons causes release of energy in the form of radiation. However this recombination is not instantaneous, meaning that many free electrons and positive ions travel freely in the upper part of Earth's atmosphere. The amount of electrons per unit volume, the electron density, depends on both the neutral density of the atmosphere and on the intensity of the solar radiation, which are highly variable in both time and space.

The ionosphere extends vertically from the upper stratosphere ($\sim 50km$) to the upper exosphere ($\sim 1000km$). In standard conditions, a maximum electron density is observed in the F-layer, between 130 and 450 km (see figure 1.1). This is the layer where O^+ ions are dominant. In the F-layer, the maximum observed electron density can reach up to $10^{12}/m^{-3}$ around noon, when ionization conditions are optimal. Below the F-layer, local electron density maxima can be observed in the D and E layers where O_2^+ and NO^+ ions are predominant. Above the F layer, He and H ions are predominant and there are usually no local extrema in electron density in the vertical direction.
The region above the ionosphere is referred to as the plasmaphere. This region is mostly made of cold plasma outflow (electrons and ions) from the underlying ionosphere, which follow the geomagnetic field lines [2].

1.2. Space weather and GNSS applications

Radio waves are greatly affected by the ionosphere because of the changing refractive index along their travel path. The presence of electrons along a wavepath causes both wave bending and delay, which affect the quality of global positioning systems. Therefore it is important to know the spatio-temporal evolution of the electron concentration in the ionosphere and plasmasphere for high accuracy positioning applications.

The current operational Global Navigation Satellite Systems (GNSS) constellation is composed of almost 100 operational satellites in Medium-Earth-Orbit (MEO) at approximately 20 000 km altitude, including 31 GPS satellites, 24 GLONASS satellites and 14 Galileo satellites. The ground GPS network is currently composed of more than 500 permanent International GNSS Service (IGS) stations. Furthermore, there are at this date more than 500 operational satellites in Low-Earth-Orbit (LEO), at approximately 500 km altitude, which are continuously tracking at least 4 different GNSS satellites

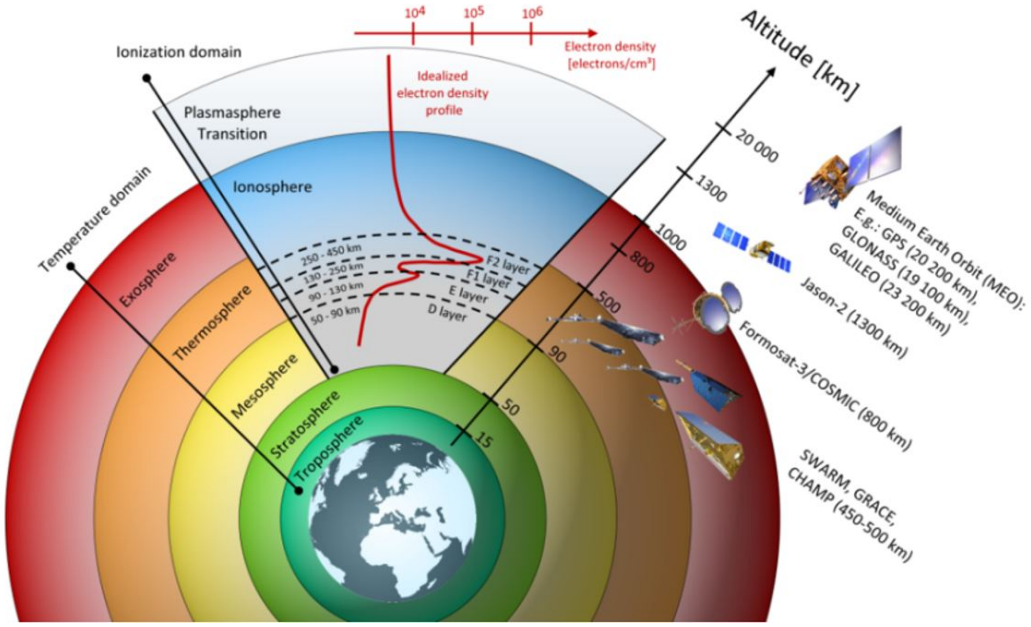

Figure 1.1: Layers of the atmosphere: classification based on the temperature (left), and based on the degree on ionisation (mid); vertical variation of the electron density within the ionosphere ans plasmasphere; orbit heights of selected satellites and satellite missions (right). **Credits : GFZ Helmholtz-Zentrum Potsdam**

for positioning purposes. Most of these GNSS antennas record both pseudo-range and phase of the GNSS signal, emitted by GNSS satellites (pseudo-range), at two different frequencies. This means that there are about $2 \times 500 \times 4 = 4000$ dual frequency pseudo-range and phase measurements with a different geometry, every 10 seconds. Every single one of these measurements is affected by the presence of electrons in the ionosphere and plasmasphere.

The question is how can the GNSS integral measurements from LEO satellite receivers be used for the retrieval of the 3D electron density in the ionosphere and plasmasphere ? Furthermore, what does it take to efficiently combine all the independent data-sets in order to increase the quality of space weather products? Space weather products, such as maps of electron density in the ionosphere and plasmasphere may then be used for improving the ground to satellite communications by correcting for the radio delay. Moreover, these observation may also be used for improving the quality of modelling the future state of the ionosphere by providing global initialisation and verification data.

2

GNSS data and retrieval methods for electron content

2.1. Measurements geometries

Dual frequency measurements of both pseudo-ranges and phases are recorded at least once every 10 seconds in an ever-growing vast network of GPS ground receivers and Low-Earth-Orbiting (LEO) satellites. GNSS satellites and LEO satellites form a tomographic network of moving emitters and receivers, separated by an unknown complex medium : the ionosphere. Due to the perpetual motion the sources and receivers, every radio signal wavepath has a sensibly different geometry in the 3D space. Three different geometries can distinguished (see figure 2.1): 1) The GNSS to ground receiver geometry, 2) the positive-elevation GNSS to LEO geometry and 3) the negative-elevation GNSS to LEO geometry, also called Radio Occultation (RO) geometry. Radio signals following all these geometries have in common that they propagate through the ionosphere and the plasmasphere, but they differ by the total distance and the angle they propagate through these dispersive media. We will mainly focus on the second type: the non RO GNSS to LEO geometry, while keeping in mind that more geometries are available for further processing.

2.2. Retrieval of Total Electron Content (TEC)

The pseudo-range is the absolute measurement of group delay between the time a signal is transmitted and received [3], given in units distance. At first order, and if bending effects caused by changing refractive indexes are ignored, the pseudo-range and phase measurements for L1 and L2 frequencies in the L band (1-2 GHz) can be modelled as:

$$P_k^i = \rho^i + \delta^i + 40.3\frac{TEC^i}{f_k^2} + C^E + C^R + \sigma_k^i \tag{2.1}$$

$$L_k^i = -\frac{c}{f_k}\Phi_k^i = n_k^i\lambda_k + \rho^i + \delta^i - 40.3\frac{TEC^i}{f_k^2} + C^E + C^R + \epsilon_k^i \tag{2.2}$$

with

- i the measurement number
- $k = 1$ or 2 for L1 or L2 frequencies respectively;
- P_k^i the i^{th} recorded pseudo-range between the emitter E and the receiver R;
- ρ^i the range corresponding to the light travel time in vacuum between the emitter and the receiver
- δ_k^i the delay caused by the neutral atmosphere;

- TEC_k^i the slant total (integrated) electron content along the wavepath, expressed in m^-2;
- 40.3 is a constant depending to the square of the plasma frequency divided by the electron density, expressed in $Hz^2.m^{-2}$;
- C^E and C^R the emitter and receiver clock errors;
- σ_k^i the measurement errors (including thermal noise, multipath...);
- L_k^i the recorded phase between the transmitter and the receiver in units distance;
- c the speed of light in vacuum;
- Φ_k^i the recorded phase in cycles;
- n_k^i an integer, source of phase ambiguity;
- λ_k the operating wavelength;
- f_k the operating frequency;
- ϵ_k^i the phase measurement noise.

Equations 2.1 and 2.2 demonstrate how much the integrated electron content between the transmitter and the receiver affects the pseudo-range and phase measurements. For instance, a Total Electron Content (TEC) of $10\,TECU(=10^{16}\,el.m^{-2})$ translates into an increased pseudo-range of 1.62 m at the

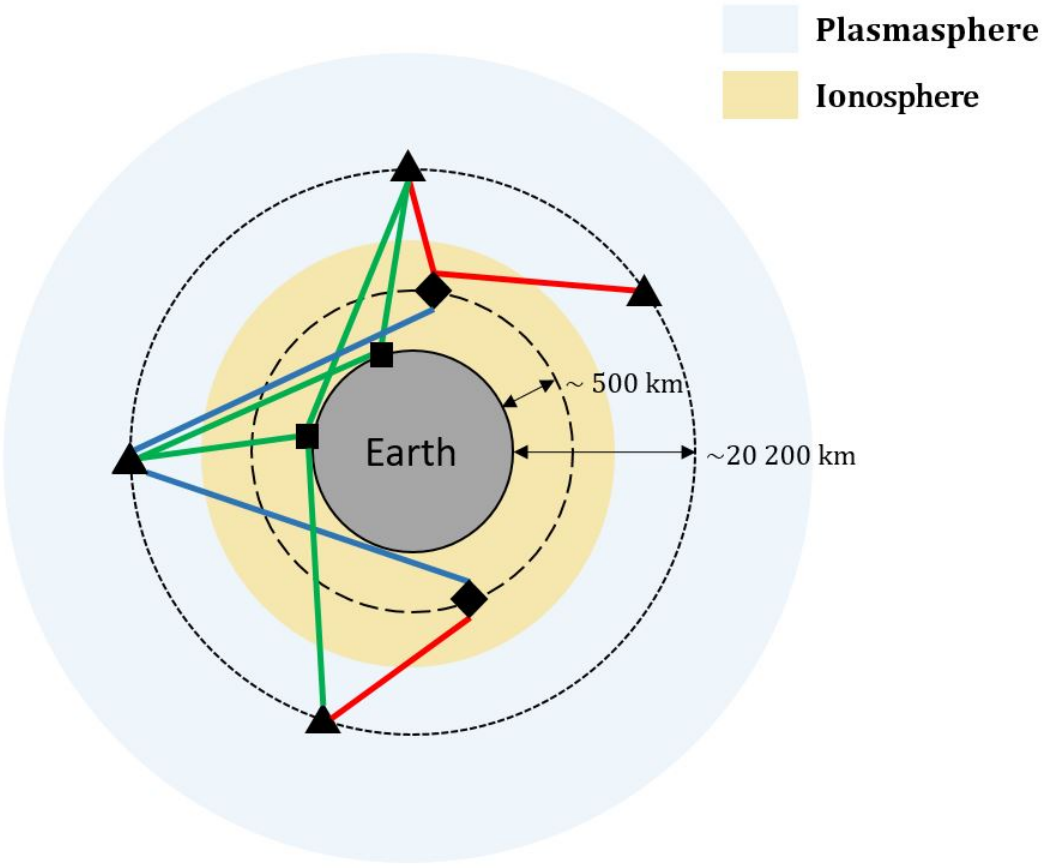

Figure 2.1: GNSS observation geometries between GNSS satellites (triangles), LEO satellites (diamonds) and ground stations (squares). The green lines are **GNSS to ground geometries**, the red lines are **positive-elevation GNSS to LEO observations** and the blue lines are **GNSS to LEO Radio Occultation (RO) geometries**.

L1 frequency and 2.67 m at the L2 frequency.
Given the fact that the ionosphere is a dispersive medium and that the neutral atmosphere is non dispersive at radio frequencies, the absolute total electron content TEC_a along a transmitter-receiver wavepath can be derived using a linear combination of P_1 an P_2 measurements (from equation 2.1):

$$TEC_a = \frac{1}{40.3}\frac{f_1^2 f_2^2}{(f_1^2 - f_2^2)}(P_2 - P_1) - (C^E_{P1-P2} + C^R_{P1-P2}) + \nu \tag{2.3}$$

where

- C^E_{P1-P2} and C^R_{P1-P2} are the emitter and receiver differential codes bias (DCB), respectively;
- ν is the absolute TEC noise.

The DCB is usually taken as a satellite-dependent, daily constant. The DCB of GPS satellites is estimated by different GPS processing centers, such as the Center for Orbit Determination in Europe (CODE). The DCB for the receivers has to be estimated for each receiver separately using assumptions on the state of the ionosphere. One method is to assume that a model ionosphere (e.g IRI2012 [4]) on average meets the real state of the ionosphere. Then the difference between the estimated TEC and the modelled TEC gives an estimate of the daily receiver DCB, which has been done in [5]. A more straightforward method is to shift all the TEC estimates by a constant such that the minimum observed TEC, usually observed during night-time for the small pseudo-ranges, is zero.

The TEC noise is related to the noise in both pseudo-range measurements according to:

$$\sigma_\nu = \frac{1}{40.3}\frac{f_1^2 f_2^2}{(f_1^2 - f_2^2)}\sqrt{\sigma^2_{P1} + \sigma^2_{P2}} \tag{2.4}$$

The frequency factor on the right hand side of equations 2.3 and 2.4 is equal to $9,52 \times 10^{16}$ in SI units. This means that a typical noise of 1 cm in the pseudo-range observations translates in a TEC precision of the order of 1 TECU. A relative but more precise total electron content TEC_r can be retrieved using a linear combination of phase observations at the two frequencies:

$$TEC_r = \frac{1}{40.3}\frac{f_1^2 f_2^2}{(f_1^2 - f_2^2)}(L_1 - L_2) + B + \mu \tag{2.5}$$

where

- B is an unknown bias;
- μ is the relative TEC noise.

Phase measurements tend to be 100 times less noisier than pseudo-range measurements, which means that the relative TEC can be retrieved with 0.01 TECU accuracy. A method to efficiently combine both pseudo range and phase measurements for TEC retrieval is to solve for B in equation 2.6 by a least-squares approach which minimizes $\sum(TEC_a - TEC_r)^2$ for all measurements in a connected arc [3]. This method gives a precise (< 0.01 TECU precision) and accurate ($1 - 3$ TECU bias) estimate of the TEC along the transmitter-receiver wavepath.

2.3. Tomographic inversion

2.3.1. Mathematical problem

We consider a set of I slant TEC measurements, taken in a selected time period, typically of the order of one LEO revolution period (~ 90 min). By definition, the slant TEC is the integral of the electron density along the i^{th} radio wave wavepath between the emitter E and the receiver R:

$$TEC_i = \int_{E_i}^{R_i} N(r, \theta, \phi) dl \quad for \quad i \in [1; I] \tag{2.6}$$

where N is the electron density (expressed in m^{-3}), r the altitude, θ the latitude, ϕ the longitude and l

the distance between the emitter and the receiver. The whole ionosphere and plasmasphere are then discretized in a longitude-latitude-altitude grid, with the altitude ranging from receiver altitude to GNSS satelite altitude, e.g from 400km to 20 200km. The intersection between every wavepath i and fixed altitude shells from the grid is computed. The length of the wavepath between each intersection point is then assigned to the closed voxel center and stored in the i^{th} row of the design matrix A (see figure 2.2. If we suppose that the electron density within all the J voxels is constant, the integral problem in equation 2.6 may be reformulated as:

$$TEC_i = \sum_{j=1}^{J} N_j l_{ij} \tag{2.7}$$

By combining all the I measurements, we are left with the following systems of linear equations:

$$y = A\ x + E \tag{2.8}$$

where:

- y is the Ix1 vector containing the I slant TEC observations;
- A is the IxJ design matrix containing the wavepath lengths within all the J grid voxels;
- x is the Jx1 vector containing the electron density in the J grid voxels;
- E is the Ix1 vector containing the variance errors σ_i caused by both the discretization and the noise of the measurements.

We will suppose that the errors are dominated by discretization errors, and that they are the same for all I measurements : $\sigma_i = \sigma$.

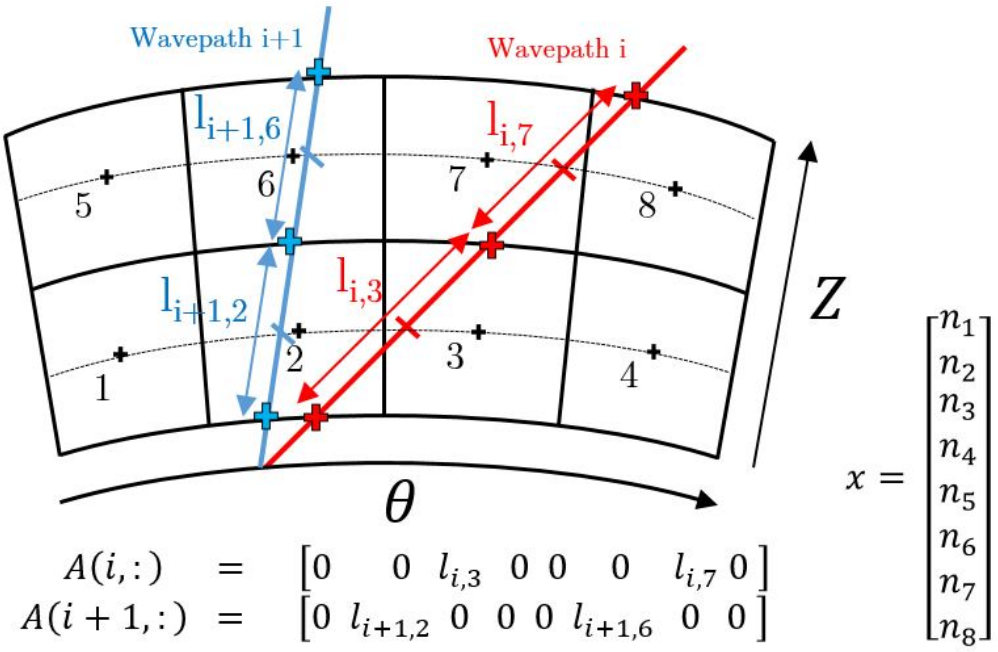

Figure 2.2: Diagram illustrating the method employed for building the design matrix **A** and the unknown electron concentration vector **x** of a 2D-simplified representation of the tomographic configuration.

2.3.2. Least squares approach

A way to solve equation 2.8 is to minimize the square of the residuals $\|y - Ax\|^2$. However, the number of observations I is much smaller than the number of electron density voxels J ($I << J$), hence equation 2.8 is under-determinded with no guaranteed solution. This translates in a A matrix that is generally simultaneously not full rank, under-determined and singular; only a subset of the I equations in equation 2.8 are linearly independent, the number of unknowns (the number of voxels J) is much larger than the number of independent equations, and the singular values of the diagonal matrix of A decrease rapidly to zero.
In this report, a $5°$, $2.5°$ grid was chosen in longitude and latitude, respectively. The altitude grid starts at LEO altitude and ranges up to 19500km, with 10km resolution near LEO altitude up to 1000km resolution at GPS altitude. This translates in at least $73 \times 73 \times 66 = 351714$ number of voxels, i.e. number of unknown electron densities.

Following [6], the number of unknowns is considerably reduced by approximating the unknown 3D electron density function at a particular time as a finite sum of spherical harmonics in the horizontal direction and empirical orthogonal functions (EOFs) in the vertical direction:

$$n(r, \theta^c, \lambda) \approx \sum_{k=1}^{K} \sum_{l=0}^{L_{max}} \sum_{m=-l}^{l} C_{lm}^k Y_{lm}(\theta^c, \phi) Z_k(r) \tag{2.9}$$

where C_{lm}^k are the unknown Fourier coefficients; $Y_{lm}(\theta, \phi)$ are the surface spherical harmonics of degree l and order m evaluated at co-latitude θ^c and longitude λ; $Z_k(r)$ is the k^{th} empirical orthogonal function (EOF) evaluated at altitude r. The spherical harmonics are written:

$$Y_{lm}(\theta^c, \phi) = P_{l,|m|}(cos\theta) \begin{cases} cos(m\phi), & \text{if } m \geq 0 \\ sin(|m|\phi), & \text{if } m < 0 \end{cases} \tag{2.10}$$

where $P_{l,|m|}$ are the 4-pi normalized associated Legendre functions. The amount of unknowns M depends strongly on the maximum degree L_{max} and on the amount of vertical EOFs K:

$$M = K \times (L_{max}^2 + 2L_{max} + 1) \tag{2.11}$$

The vertical EOFs are obtained using the IRI-2012 model of the ionosphere, which provides us with modelled values of electron concentration up to an altitude of 2000km. However, the total measured TEC is also greatly affected by the plasmasphere, between 2000km and GPS height (~ 20000km) [7]. For this purpose a simple exponential model was used to model plasmaspheric electron concentration:

$$n^P(r) = n_0^P exp(-(r - 2000)/H_p) \quad for \quad r \in [2 \times 10^3; 2 \times 10^4] \quad (km) \tag{2.12}$$

where n_0^P is the electron concentration at 2000 km, given by IRI-2012, and H_p is the plasmasphere scale height parameter, fixed at a value of 3000km. The modelled electron concentration in the $73 \times 73 \times 66$ grid is then used to make several electron concentration profiles, which are then stored in the columns of a matrix. The eigen-analysis of the covariance matrix of all the profiles gives the K right eigenvectors, which are used as the K EOFs. The amount of EOFs, K, is chosen such that the maximum variability of the electron concentration in the vertical is captured, while minimizing the amount of unknowns according to equation 2.11.
The measured slant TEC can then be written as a finite sum of 66 electron densities in the vertical direction:

$$TEC_i = \sum_{j=1}^{66} l_{ij} \sum_{k=1}^{K} \sum_{l=0}^{L_{max}} \sum_{m=-l}^{l} C_{lm}^k Y_{lm}(\theta_{ij}^c, \phi_{ij}) Z_k(r_{ij}) \tag{2.13}$$

$$\Leftrightarrow TEC_j = \sum_{k=1}^{K} \sum_{l=0}^{L_{max}} \sum_{m=-l}^{l} C_{lm}^k \sum_{j=1}^{66} l_{ij} Y_{lm}(\theta_{ij}^c, \phi_{ij}) Z_k(r_{ij}) \tag{2.14}$$

If we denote the triple summation over indexes k, l and m as one larger sum of M indexes:

$$\sum_{k=1}^{K}\sum_{l=0}^{L_{max}}\sum_{m=-l}^{l} = \sum_{k,l,m=1}^{M} \tag{2.15}$$

then the slant TEC becomes:

$$TEC_i = \sum_{k,l,m=1}^{M} C_{lm}^{k}\sum_{j=1}^{55} l_{ij}Y_{lm}(\theta_{ij}^{c},\phi_{ij})Z_k(r_{ij}) \tag{2.16}$$

where θ_{ij}^{c}, λ_{ij} and r_{ij} are the co-latitude, longitude and altitude of the j^{th} center between two consecutive intersections of the i^{th} LEO to GNSS wavepath and the fixed altitude shells (see figure 2.2). And l_{ij} is the j^{th} length of the i^{th} wavepath between two intersection points.

In matrix form, and expanded for all measured slant TEC, the forward problem expressed in equation 2.8 may be rewritten (following the notation in [8]):

$$y \quad = \quad AX \quad \times \quad W \quad + \quad E \tag{2.17}$$

where

- y is the Ix1 vector containing the I slant TEC observations;
- AX is the IxM design matrix;
- W is the Mx1 vector containing the M unknown coefficients C_{lm}^{k} ;
- E is the Ix1 vector containing the variance errors σ_i caused by both discretization and measurement noise.

Each column of AX contains the weighted contribution of all 66 known harmonic functions of index (k,l,m), $Y_{lm}(\theta_i,\lambda_i)Z_k(z_{ij})$, summed over all altitudes, to the unknown coefficient C_{lm}^{k}. If we use $K = 3$ vertical EOFs, and horizontal spherical harmonics up to degree and order $L_{max} = 25$, then the harmonic decomposition of the electron density has reduced the amount of unknowns to estimate from 351714 to 2028. However, even though there are enough independent equations to solve the problem (AX is full rank), the matrix is still highly singular, meaning that the least-squares solution will be dominated by errors caused by the discretization of the continuous problem expressed in equation 2.6. This manifests itself by the degeneracy of the singular values of the diagonal matrix of AX.

The singular value decomposition (SVD) of matrix AX may be written as:

$$AX \quad = \quad U \quad \Lambda \quad V^T \tag{2.18}$$

where:

- U is the I matrix containing the first P left singular vectors in each column;
- Λ is the $P \times P$ diagonal matrix containing the P non-zero singular values λ_p of AX.
- V is the $M \times P$ matrix containing the first P right singular vectors in each column.

The index P is chosen such that the matrix Λ is a square diagonal matrix filled with strictly positive values, hence Λ is invertible. The least-squares solution for the system may then be written as:

$$\hat{W} = V\Lambda^{-1}U^T y \tag{2.19}$$

and the solution covariance as:

$$cov(\hat{W}) = \sigma^2 V\Lambda^{-2}V^T \tag{2.20}$$

According to equation 2.20, the covariance of the solution increases rapidly due the very small singular values stored in Λ. At the same time, the more singular values we incorporate in the least squares

solution, the closer we get to the true solution, according to equation 2.19. One way to overcome this problem would be to perform a singular value cutoff and keeping only the equations in 2.19 that involve singular values above a certain threshold λ_k. The value of the chosen threshold depends on the amount of noise in the data σ and on the desired quality of the estimation $\sigma_{\hat{W}}$. For instance, a SV cutoff λ_k of 1000km would cause a typical TEC noise σ of $10^{16}m^{-2}$ to propagate in a noise $\sigma_{\hat{W}}$ of $10^{10}m^{-3}$.

To conclude, a trade-off value for the filter singular value index must be chosen such that both the covariance and the residuals of the solution are minimal. The cutoff index depends on the amount of noise in the data, on the quality of the discretization and on the geometry and on the amount of data.

3

3D electron density retrieval in the upper ionosphere and plasmasphere

In this section, the results of the 3D retrieval algorithm, discussed in section **??** using a reduced data-set, are presented.

3.1. Data and methods

Navigation and positive-elevation GNSS data collected on March 17th 2015 from the GRACE[1] and the SWARM[2] missions have been used. The daily navigation data and GNSS data from the GRACE mission are sampled in 5s and 10s data-sets respectively, whereas the navigation and GNSS data from the SWARM mission are both sampled in 1s data-sets. These data-sets have all been re-sampled in 10s data in order to be used together. Then the 15 min IGS precise GPS orbits[3] were interpolated into 10s precise orbits. The slant absolute TEC was estimated for every GNSS measurement using the L1 and L2 pseudo-ranges using equation 2.3. The slant TEC estimates were corrected for emitter clock errors using the monthly estimated differential code biases (DCB) from CODE[4]. P1 and P2 pseudo-range observations with a signal to noise ratio below 20 dB are then removed. Finally, the daily receiver DCB was corrected by removing an arbitrary constant value such that the observed TEC are always strictly positive.

The two GRACE satellites have a circular orbit, with an inclination of $89°$ and travel at an altitude between 400 and 450km. The SWARM constellation flies also in a circular orbit with an inclination of $87.5°$. The SWARM-A, SWARM-B satellites travel at an altitude of 450-470 and the SWARM-C travels at an altitude of 500-520km (see figure 3.1). An abnormal solar activity lead to the arrival of coronal mass ejection at 04:45 UTC on 17/03/2015 [9]. The series of interactions with the Earth's atmospheric layers eventually lead to abnormal values of vertical total electron concentration (VTEC) all around the globe. The focus will be on the South-American sector, in the time period ranging from 23:10 until 23:45 UTC on 17/03/2015, where abnormal high values of VTEC were observed.
In the next part, only results involving SWARM-A and SWARM-C data are shown. Different data-sets were used but the combination of SWARM and GRACE data proved difficult as arbitrary corrections have been applied to the data. Moreover, combining data-sets from satellites at different altitudes is challenging due to the important electron concentrations at these altitudes.

The vertical variability of the electron concentration can be seen in Figures 3.2 and 3.3. The maximum electron density is expected at tropical latitudes and at altitudes between 300km and 400km,

[1]data from GFZ and downloaded from ftp://rz-vm152.gfz-potsdam.de/
[2]data from ESA and downloaded from https://earth.esa.int/web/guest/home
[3]data from NASA and downloaded from ftp://cddis.gsfc.nasa.gov/gnss/products/
[4]data from CODE and downloaded from ftp://ftp.unibe.ch/aiub/CODE/

which corresponds to the ionospheric F-layer. The considered LEO satellites travel above this maximum, hence we expect ionospheric concentrations to monotonically decrease with altitude from LEO height. The maximum electron density along the GPS to LEO path strongly depends on the local time (see figure 3.1), and varies between $2.10^{12}m^{-3}$ near the equator during daytime and $5.10^{10}m^{-3}$ at higher latitudes, during nighttime.

The reduction of unknowns was performed using a spherical harmonics expansion up to degree and order 25 ($l_{max} = 25$) of the electron density in the horizontal directions and one ($K = 1$) empirical orthogonal function (EOFs) for the vertical direction. This mapping reduces the number of unknowns

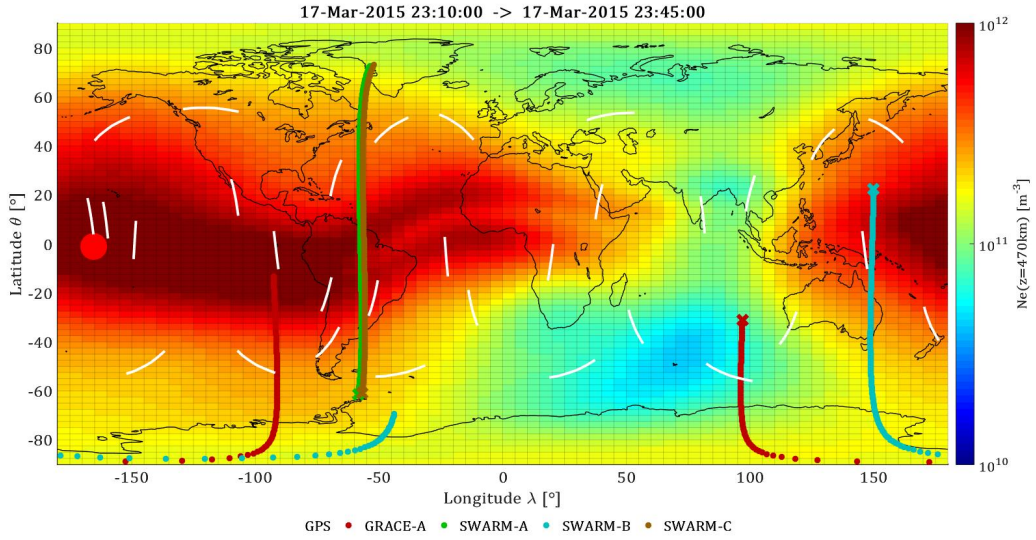

Figure 3.1: SWARM, GRACE and GPS orbits between 23:10 and 23:45 UTC on March 17th, 2015. The white lines are the all the GPS orbits during this time period. The colored crosses represent the starting positions of the corresponding satellites at 23:10 UTC. The background color corresponds to the electron density at 470km altitude, modelled by the IRI-2012 model on the same day at 23:00 UTC. The red circle denotes the position of the sun in ECEF coordinates at 23:00 UTC.

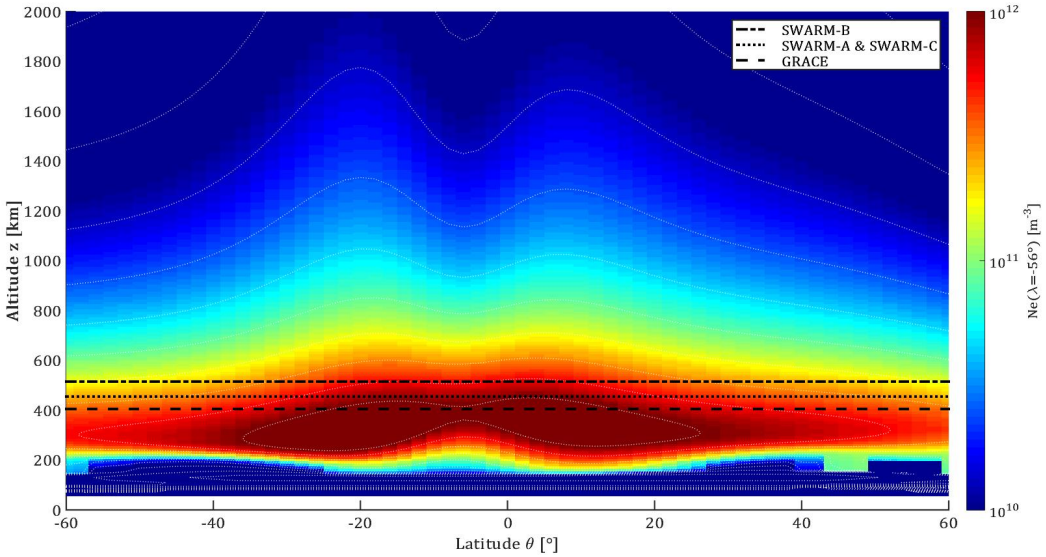

Figure 3.2: SWARM and GRACE orbit altitudes on March 17th, 2015 . The background color corresponds to the electron density at 56 longitude, modelled by IRI-2012 on the same day at 23:00 UTC. The dashed white lines are constant electron density lines.

from $73 \times 73 \times 66 = 391314$ voxels to $M = 1 \times (25^2 + 2 \times 25 + 1) = 676$ Fourier coefficients, hence the size of the problem is considerably reduced. Reconstructions using more EOFs were implemented, but the least square solution lead to negative electron densities. This might be due to the data-set that to a certain extent both biased and noisy, hence the least square estimation uses the vertical variability stored in the different EOFs in order to correct for imperfect dataset.

The mathematical problem, written down in equation 2.8, was solved using the truncated least-squares approach described in the previous section and using three different data-sets for comparison: first using SWARM-A data, then using SWARM-C data and finally using the two data-sets combined.
The degeneracy of the singular values in the diagonal matrix Λ is shown in figure 3.4. The degeneracy of the singular values stored in the Λ matrix is slightly reduced by combining the two separate data-sets. The observed range of singular values ($10^8 m$ to $10^{-10} m$) means that a slant TEC noise of 1 TECU propagates in a Fourier coefficients noise increasing from $10^8 m^{-3}$ to $10^{26} m^{-3}$, depending on the amount of chosen singular values. The norm of the least squares solution versus the norm of the residuals using a range of singular value (SV) cutoff values has been drafted in figure 3.5. SV indexes higher than 34 cause the norm of the solution to increase rapidly, while SV indexes below 34 cause a rapid increase in the residuals. Hence a cutoff value of $j_{max} = 34$, corresponding to a SV close to 5000km, was chosen for further estimation. This solution is close to minimum-norm solution. This indicates that using a perturbation electron density field to some a-priori model might yield better estimation results, as we don't expect the true electron density field to be of minimum norm. The reason this amount of filtering was used is that less filtering yields unrealistic values of electron density, which is most likely caused by the noise in the slant TEC data-set.

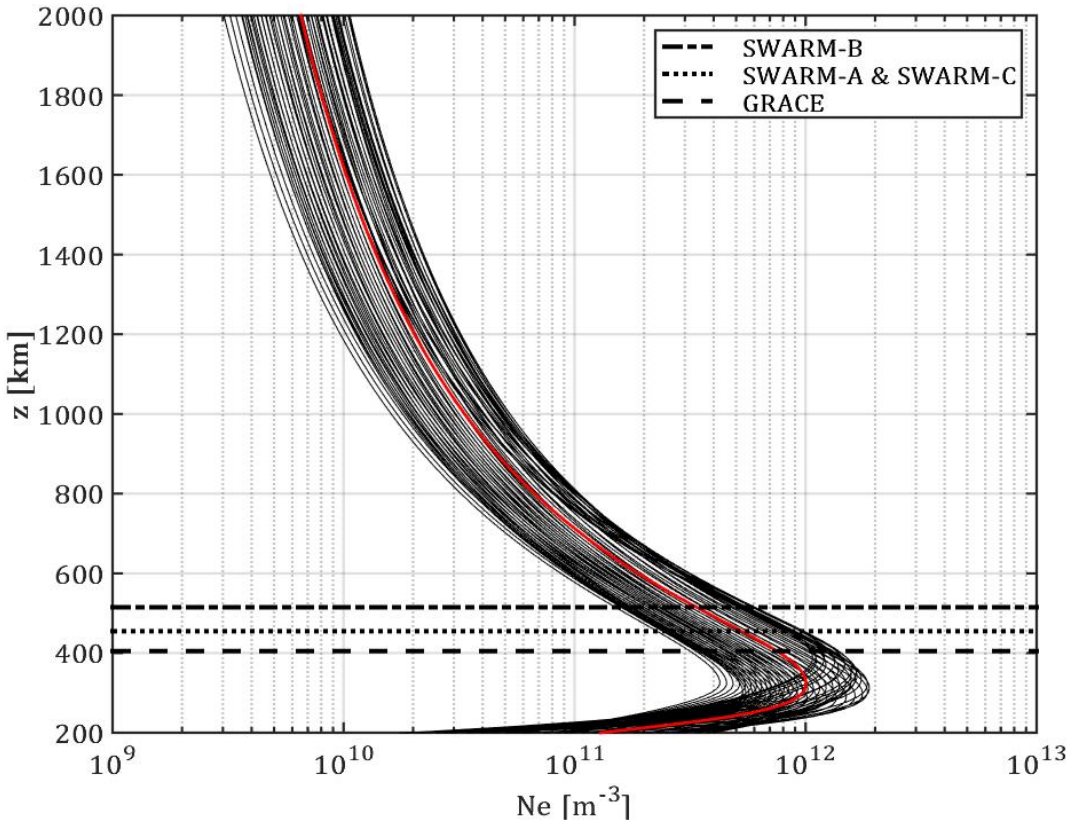

Figure 3.3: Ionospheric electron density profiles from IRI-2012 for latitudes ranging from $-60°$ to $60°$ and for $-56°$ longitude on March, 17th 2015 at 23:00 UTC. The thick red line is the mean profile for this data-set. The horizontal lines are the mean altitudes of the GRACE and SWARM missions on this day.

3.2. Results

The estimated Fourier coefficients using the truncated least squares approach were then used to reconstruct the estimated electron density in the near vicinity of the wavepath intersections. During the selected period, the SWARM satellites travel at a almost constant longitude (see figure 3.1). Hence the electron density was only reconstructed for a very small range of longitudes, ranging from -60 to -55 °. The result is shown in figure 3.6. The least squares estimation is able to capture the horizontal and

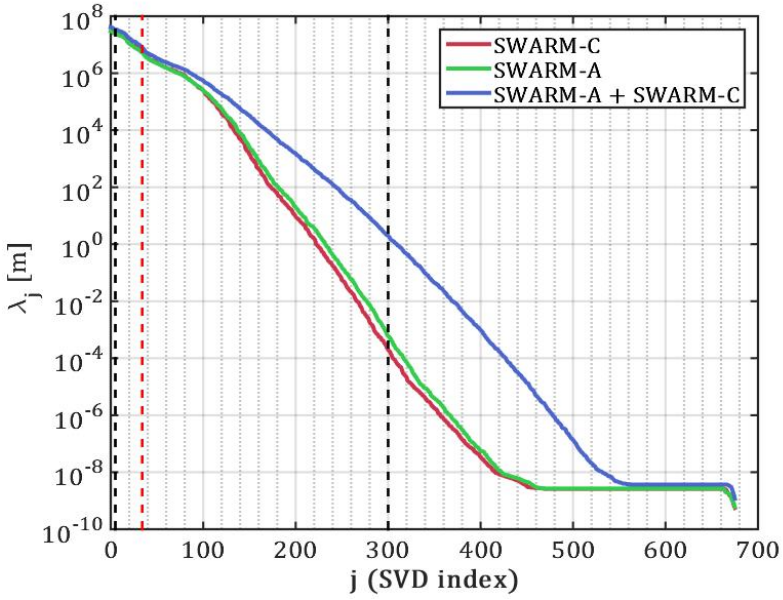

Figure 3.4: Picard plot of the diagonal matrix of the design matrix AX using three different slant TEC datasets between 23:10 and 23:45 UTC on 17/03/2015. The dashed black vertical lines represent the minimum (5) and maximum (300) cutoff indexes that were implemented for the truncated least squares estimation. The dashed red vertical line represents the used cutoff index (34).

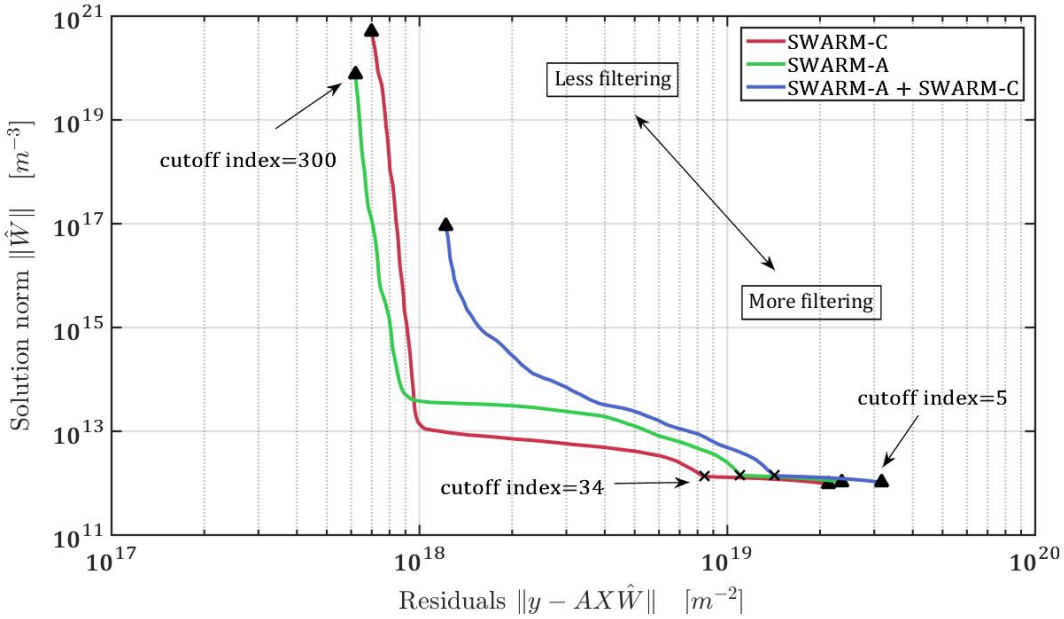

Figure 3.5: Scatter plot of norm the estimated Fourier coefficients versus the norm of the least squares residuals for singular value (SV) cutoff indexes ranging from 5 to 300, and for three different slant TEC datasets between 23:10 and 23:45 UTC on 17/03/2015. The black crosses are located at the chosen SV index of 34.

vertical electron density features found in the IRI-2012 model. The two local electron density maxima at $-20°$ and $5°$ latitude are found in all the reconstructed density fields.
The differences between reconstruction and model are shown in figure 3.7. The relative difference between reconstructions using different data-sets is small, which is an indication of the consistency in the reconstructed electron density. Furthermore, the vertical variability between model and reconstruction is the same, as the EOFs for the least squares retrieval were derived from this model. This means that the estimation procedure will be much less sensitive to electron density changes in the vertical that are not captured by the model. In this case, only one EOF was used for the vertical variability, meaning that the least squares estimation constrains the solution to have a vertical electron density profile described by the model.

However, there are also strong differences. There is approximately a factor 10 difference between reconstructed and modelled electron density, which might be related to the abnormal ionospheric conditions on this date, as the IRI 2012 model was ran for normal conditions. The absolute differences are most important at lower altitudes, where concentrations are higher. On the other hand, the relative differences show important gradients in the horizontal direction. This is related to the fact that LEO satellite data is very sensitive to changes in electron concentration in the horizontal direction, hence the retrieved electron density shows horizontal features that are not found in the model. The reconstruction is able to detect horizontal structures of $\sim 10°$ size in latitude, whereas the model only detect features approximately twice that size. This demonstrates that the IRI model might not be appropriate for representing the ionosphere on smaller horizontal scales. For instance, the reconstruction finds a drop in electron densities at $40°$ latitude that is invisible in the model.

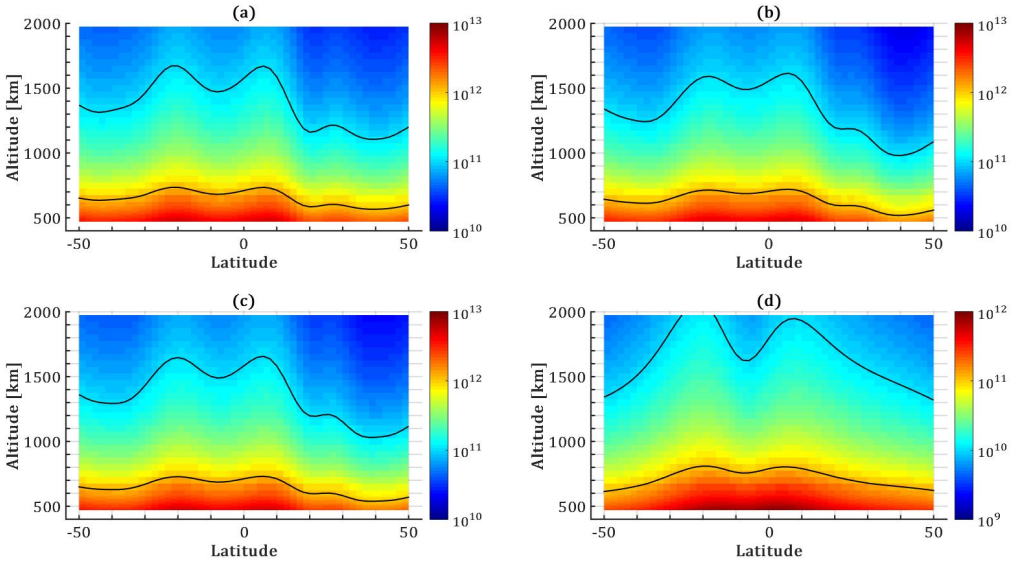

Figure 3.6: Result of electron density distribution in m^{-3} using (a) SWARM-A data, (b) SWARM-C data and (c) both SWARM-A and SWARM-C data together between 23:10 and 23:45 UTC on 17/03/2015 at $-59°$ longitude. The output of the IRI-2012 model is shown in (d). Note the different color mapping scale in (d). Contour levels are shown for every multiple of 10.

Finally, the vertical total electron content (VTEC) is computed from the reconstructed 3D density field and shown in figure 3.8. The modelled VTEC is consistent with the VTEC reconstructed with a single layer ionosphere assumption from [9]. The reconstruction, however, is only able to model the density field close to the satellite's trajectory, thus more data-sets are required for a global mapping of 3D density.

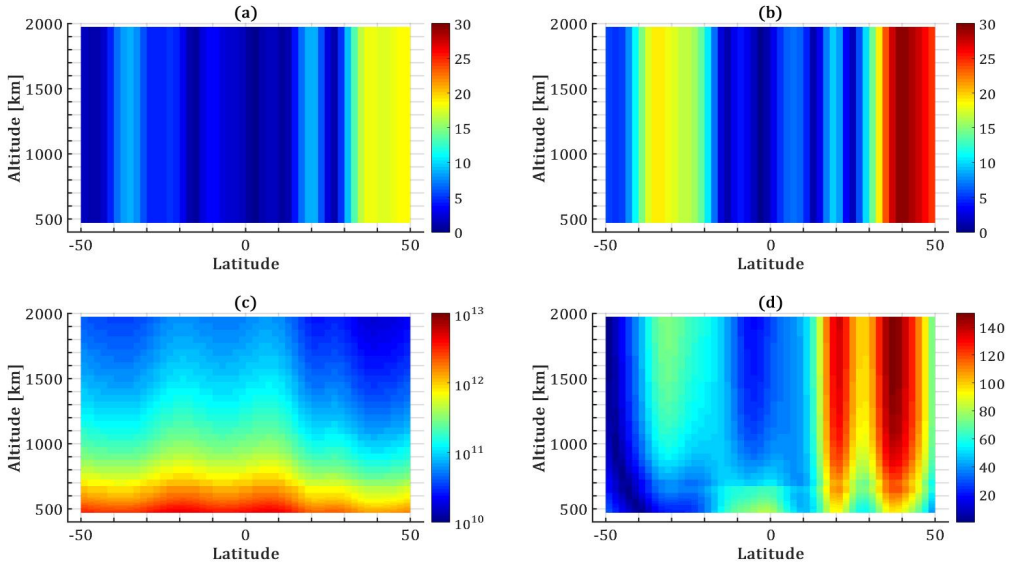

Figure 3.7: Relative difference in retrieved electron density between (a) (SWARM-A) data and (SWARM-A + SWARM-C) data and between (b) (SWARM-A) data and (SWARM-C) data, expressed in %. The absolute difference in m^{-3} between retrieved electron density using (SWARM-A + SWARM-C) data and the output of the IRI-2012 model is shown in (c). The relative difference in % between (SWARM-A + SWARM-C) data and 10 times the output of the IRI-2012 model is shown in (d).

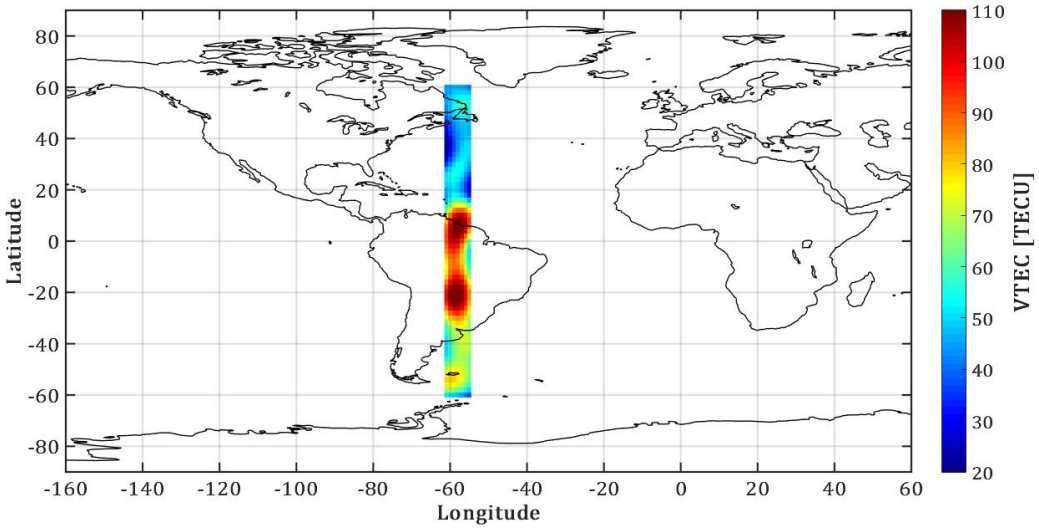

Figure 3.8: Reconstructed vertical total electron content (VTEC) between 470 km and 20 000 km altitude expressed in TECU (= $10^{16} m^{-2}$), between 23:10 and 23:45 UTC on 17/03/2015 and using SWARM-A data.

4

Conclusion and suggestions

4.1. Conclusion

The dispersive properties of free-electrons in the L band have been exploited to transform the recorded dual-frequency pseudo-ranges from different LEO satellites into slant total electron content. The integral measurements between moving emitters (GPS satellites) and moving receivers (LEO satellites) have been used in a tomographic least squares estimation algorithm in order to extract the 3D electron density in the complex medium, which is made of both the upper ionosphere and the plasmasphere (see figure 4.1).
The results show that these data-sets can be used to find high frequency horizontal features in electron density. The lack of horizontal wavepath geometries within the ionosphere translates in a poor vertical resolution, hence assumptions on the vertical profile are required for the retrieval of the vertical electron density. Nevertheless, the reconstructed 3D electron density field can be used to correct for the ionospheric radio delay without using the commonly used single-layer ionosphere assumption [10].
Several near real-time LEO satellite data-sets can be combined to make global maps of 3D electron density. Global 3D mapping of ionospheric and plasmaspheric electron content might reveal useful for model assimilation purposes, hence for improving the quality of space weather predictions.

4.2. Challenges and suggestions

This study has revealed some challenges that need to be considered when using LEO navigation data for ionospheric modelling purposes:

1) All low earth orbiting satellites travel at different altitudes, which makes the combination of these different data-sets challenging as a different discretization is required. In addition, the influence of the free electrons present inside the ionosphere cannot be neglected at these altitudes.

2) The emitter clock errors need to be corrected for every single receiver independently and with great accuracy, otherwise the different data-sets cannot be used together due to different unknown biases in the data.

3) The assumption of a ionosphere constant in time might no longer be valid for long time periods or during solar storms. The electron concentrations $n(r, \theta, \phi)$ is also a function of time.

4) The geometry of the satellites requires the use of assumptions on the vertical profile of the electron density. In this study, the vertical resolution of the electron density reconstruction is non existent due to the use of only one empirical orthonormal function (EOF) in the vertical direction. More EOFs were used but the increased vertical variability tends to generate non realistic values of electron density, which is most likely caused by the noise of the data.

The first two challenges can be avoided by processing each data-set independently. This would give global coverage if enough receivers are used, however the different reconstructed density fields might not be consistent due to different data and discretization errors. Additionally, using small time

windows (e.g 20min) can be used to minimize the errors caused by the time dependent ionosphere. Finally, different assumptions of the vertical electron density profile can be used to increase the quality of the retrieval in the vertical direction. For instance, electron density in the plasmasphere can be forced to be constant along the magnetic field lines, as has been done in [11].

Finally, both the signal and the noise are expected to be lower during more quiet conditions. Hence it might also be interesting to look at data-sets during quiet solar conditions in order to assess the quality of this retrieval method for lower values of electron density. Moreover, the IRI model and the least-squares method should be very similar in such a situation.

In this work, only positive-elevation GNSS data-sets from 4 LEO satellites were used for solving the tomographic problem. Many more data-sets and different geometries can be considered as well, in particular the radio occultation (RO) geometries, which offer a way to extract the lower ionosphere density profile. Together with data from ground stations, the whole ionosphere, from top to bottom, could then be imaged in 3D on a global scale.

Real time imaging of the ionosphere in 3D can be very useful to correct the radio delays of single receiver antennas. This study, using a simplified retrieval methods and a limited data-set, has already demonstrated that the results are of higher spatial resolution than the widely used IRI model. Furthermore, corrections using 3D models do not require the single layer ionosphere assumption, commonly used for corrections using VTEC maps but important source of error. Real-time 3D imaging is possible if data and precise orbits from GNSS and LEO satellites are directly available (see figure 4.1). The data-sets from many different LEO satellites only need minor pre-processing steps, such as re-sampling, outlier removal, quality control, and RINEX and SP3 format version conversion, before being inserted in one common database. This common database can then be used as input for the least-squares estimation of 3D electron density.

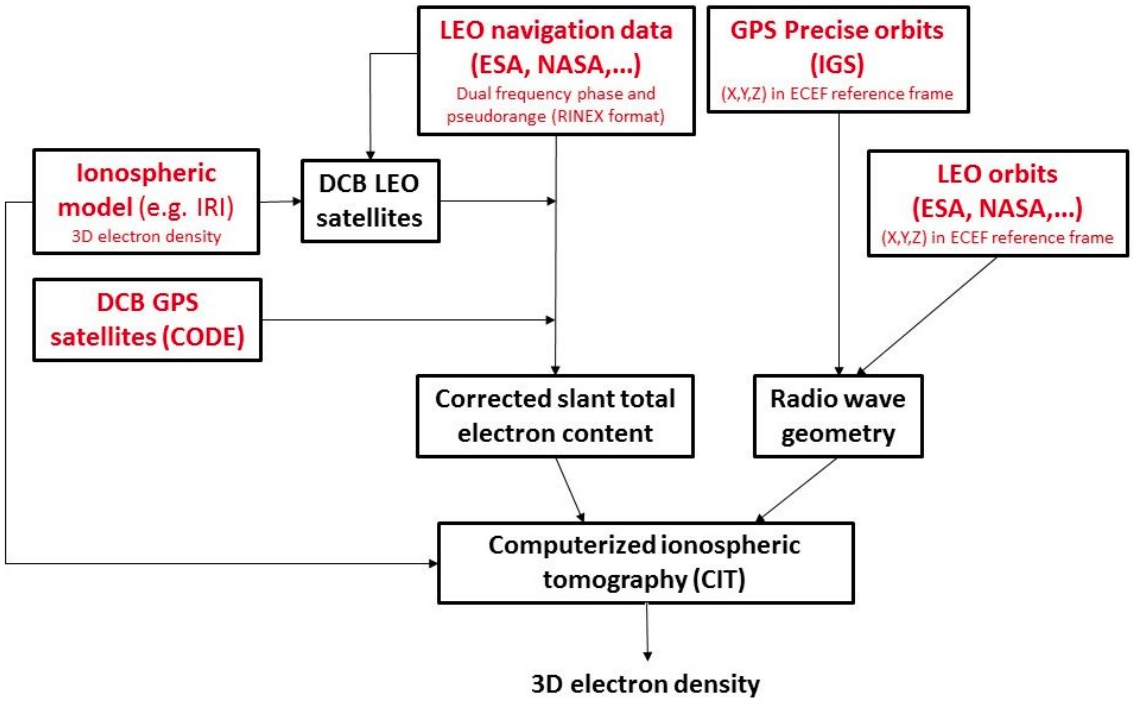

Figure 4.1: Overview of processing steps required for estimating the 3D electron density using radio navigation data between Low-Earth-Orbiting (LEO) satellites and GPS satellites.

4.3. Acknowledgements

I thank Dr. Ir. Sandra Verhagen for the good advice and for supervising this report. I thank Prof. Dr. Pier Siebesma for the taking the time understanding and assessing the quality of this additional thesis. I also thank Dr. Ir Eelco Doornbos for the guidance regarding the use of the SWARM and GRACE data-sets, and Dr. Ir. Peter de Bakker for the help with processing the GNSS navigation data. This rather short but intensive project was a good opportunity for me to familiarize myself with both imaging a complex medium and processing large data-sets. The objectives of this project were fairly ambitious, and I found that it is not always easy to drop some parts of the research for the sake of time. From a personal perspective, this project made me realize that a research project never really is finished, and that a lot of compromises and choices need to be made for writing the report in a timely manner.

Bibliography

[1] *I introductory and background material,* in *The Earth's Ionosphere — Plasma Physics and Electrodynamics* (Elsevier BV, 2009) pp. 1–26.

[2] J. Lemaire, K. Gringauz, D. Carpenter, and V. Bassolo, *The Earth's Plasmasphere*, Cambridge Atmospheric and Space Science Series (Cambridge University Press, 2005).

[3] G. A. Hajj, L. C. Lee, X. Pi, L. J. Romans, W. S. Schreiner, P. R. Straus, and C. Wang, *COSMIC GPS ionospheric sensing and space weather,* Terrestrial, Atmospheric and Oceanic Sciences **11**, 235 (2000).

[4] D. Bilitza, D. Altadill, Y. Zhang, C. Mertens, V. Truhlik, P. Richards, L.-A. McKinnell, and B. Reinisch, *The international reference ionosphere 2012 – a model of international collaboration,* Journal of Space Weather and Space Climate **4**, A07 (2014).

[5] S. Heise, N. Jakowski, A. Wehrenpfennig, C. Reigber, and H. Lühr, *Sounding of the topside ionosphere/plasmasphere based on GPS measurements from CHAMP: Initial results,* Geophysical Research Letters **29**, 44 (2002).

[6] B. M. Howe, K. Runciman, and J. A. Secan, *Tomography of the ionosphere: Four-dimensional simulations,* Radio Science **33**, 109 (1998).

[7] E. Yizengaw, M. Moldwin, D. Galvan, B. Iijima, A. Komjathy, and A. Mannucci, *Global plasmaspheric TEC and its relative contribution to GPS TEC,* Journal of Atmospheric and Solar-Terrestrial Physics **70**, 1541 (2008).

[8] C. N. Mitchell and P. S. J. Spencer, *A three-dimensional time-dependent algorithm for ionospheric imaging using gps,* Annals of Geophysics **46** (2003), 10.4401/ag-4373.

[9] E. Astafyeva, I. Zakharenkova, and M. Förster, *Ionospheric response to the 2015 st. patrick's day storm: A global multi-instrumental overview,* Journal of Geophysical Research: Space Physics **120**, 9023 (2015).

[10] D. J. Allain and C. N. Mitchell, *Ionospheric delay corrections for single-frequency GPS receivers over europe using tomographic mapping,* GPS Solutions **13**, 141 (2008).

[11] P. S. J. Spencer and C. N. Mitchell, *Imaging of 3-d plasmaspheric electron density using GPS to LEO satellite differential phase observations,* Radio Science **46**, n/a (2011).